

Experiments in Fluids

An axisymmetric inertia-gravity wave generator

--Manuscript Draft--

Manuscript Number:	EXIF-D-17-00148
Full Title:	An axisymmetric inertia-gravity wave generator
Article Type:	Research Article
Keywords:	inertia-gravity waves; axisymmetric wave generation; wave focusing
Abstract:	<p>There has been a rich interplay between laboratory experimental studies of internal waves and advancing understanding of the role of internal waves in the ocean and atmosphere. In this study, we present and demonstrate the concept for a new form of laboratory internal wave generator that can excite axisymmetric wave fields of arbitrary radial structure. The construction and operation of the generator are detailed, and its capabilities are demonstrated through a pair of experiments using a Bessel function and a Bourrelet (i.e. ring-shaped) configuration. The results of the experiments are compared with the predictions of an accompanying analytical model.</p>

Noname manuscript No.
(will be inserted by the editor)

An axisymmetric inertia-gravity wave generator

P. Maurer ·
S.J. Ghaemsaidi ·
S. Joubaud ·
T. Peacock · P. Odier

Received: date / Accepted: date

Abstract There has been a rich interplay between laboratory experimental studies of internal waves and advancing understanding of the role of internal waves in the ocean and atmosphere. In this study, we present and demonstrate the concept for a new form of laboratory internal wave generator that can excite axisymmetric wave fields of arbitrary radial structure. The construction and operation of the generator are detailed, and its capabilities are demonstrated through a pair of experiments using a Bessel function and a *Bourrelet* (i.e. ring-shaped) configuration. The results of the experiments are compared with the predictions of an accompanying analytical model.

Keywords Inertia-gravity waves · Axisymmetric wave generation · Wave focusing

PACS 47.35.Bb · 47.55.Hd · 47.32.Ef

1 Introduction

Laboratory experimentation has a compelling history of advancing the field of internal wave dynamics. The pioneering experiments of Gortler (1943) and Mowbray and Rarity (1967) provided the first demonstration of the peculiar internal wave dispersion relation. Early experiments studying wave generation in shear

P. Maurer · S. Joubaud · P. Odier
Ecole Normale Supérieure de Lyon
46 allée d'Italie
69007 Lyon, France
Tel.: (+33) 4 72 72 85 81
E-mail: philippe.odier@ens-lyon.fr

S. J. Ghaemsaidi · T. Peacock
MIT

flows (Lee and Beardsley, 1974) evidenced the role of non linearities and dispersion. These effects were studied in situ, for example by Apel et al. (1975) using satellite observations, and much more recently by Thomas et al. (2016) using pressure sensors in the Massachusetts Bay. Another example of the interplay between laboratory experiments and oceanic internal waves was the field study by Halpern (1971), regarding internal waves produced by tidal flows, which lead to experiments by Maxworthy (1979), whose results were then utilized by a number of field studies (e.g. Haury et al. (1979)). The experiments by Cacchione and Wunsch (1974) studying the reflection of internal waves over a slope also provided explanations of diapycnal mixing observed in the ocean, such as in the Monterrey Canyon (Kunze et al., 2012). Additional examples of synergy between experiments and field observations, focussed on wave-induced mixing, can be found in the review by (Ivey et al., 2008).

The methods employed to generate internal waves in laboratory settings have evolved markedly since Gortler (1943) and Mowbray and Rarity (1967), who used an oscillating cylinder as their wave generation tool. Some prominent examples of internal wave generation mechanisms applied in the laboratory include: a single paddle extending vertically across the depth of a wave tank, which excites vertical mode structures (Cacchione and Wunsch, 1974); a paddle with a localized deformation to generate wave beams (Delisi and Orlanski, 1975); and oscillating topographic features cut from foam blocks to generate low mode dominated internal wave fields (Echeverri et al., 2009). Oscillations of the wave tank itself have been used to generate internal wave attractors (Maas et al., 1997), while wave paddles continue to be used, an example being the study of instabilities arising from intersecting wave beams (Teoh et al., 1997).

The aforementioned generation methods are characterized by a fixed spatial structure, which in turn limits experimental control over the spatial structure of the internal wave field. A major advance, therefore, was the advent of novel internal wave generation technology comprising a series of stacked plates driven by an eccentric cam shaft (Gostiaux et al., 2006), for which it is possible to configure the profile of the stacked plates to have the shape of a desired wave form. The capabilities of this novel wave generator technology were comprehensively investigated and demonstrated by Mercier et al. (2010), who used such a generator to produce several different canonical wave forms, including plane waves, wave beams of different cross sectional form and vertical modes. The versatility of this wave generator has led to its use in a multitude of

1 experiments, including studies of internal tide scatter-
 2 ing (Peacock et al., 2009), parametric subharmonic in-
 3 stability (Bourget et al., 2013; Ghaemsaidi et al., 2016;
 4 Maurer et al., 2016), propagation through non-uniform
 5 stratifications (Mathur and Peacock, 2009; Paoletti and
 6 Swinney, 2012), and bolus generation (Moore et al.,
 7 2016).

8
 9 To date, internal wave experiments have typically
 10 considered nominally two-dimensional (2D) configu-
 11 rations (i.e. assuming negligible variability across the
 12 experimental wave tank). Some experiments have
 13 looked into three dimensional (3D) effects, however,
 14 such as the generation of a conical wave field by an
 15 oscillating sphere (Ghaemsaidi and Peacock, 2013), os-
 16 cillation of an axisymmetric Gaussian topographic fea-
 17 ture (King et al., 2010), and the generation of wave
 18 beams by narrow stacked plate generators in relatively
 19 wider tanks that produce 3D mean flows (Bordes et al.,
 20 2012). In an axisymmetric configuration, Duran-Matute
 21 et al. (2013) used a torus to generate purely axisym-
 22 metric inertial waves. In this paper, we demonstrate
 23 the adaptation of a multi-plate wave generator to pro-
 24 duce robust axisymmetric wave fields of arbitrary rad-
 25 ial structure. By virtue of the underlying symmetry,
 26 this advance is also naturally conducive to incorporat-
 27 ing background rotation into the experimental investi-
 28 gations.

29
 30 We begin, in section 2, with an overview of the op-
 31 erational design of the wave generator and the exper-
 32 imental configuration, including details of the rotat-
 33 ing table facility. Then, in section 3, we present de-
 34 tails of an axisymmetric model of internal wave gen-
 35 eration and propagation that we have developed and
 36 use for comparison with the experimental wave fields.
 37 In sections 4 and 5, we present experimental results
 38 for two different configurations of the wave generator,
 39 a Bessel function and a *Bourrelet* (an axisymmetric os-
 40 cillating bump). Finally, we present our conclusions in
 41 section 6.

42 2 Experimental methods

43 2.1 Generator design

44
 45
 46 The construction of the axisymmetric wave generator
 47 follows the underlying operational principle of Gos-
 48 tiaux et al. (2006) by using a series of stacked plates
 49 forced by eccentric cams to initiate internal wave dis-
 50 turbances. The schematic and images in figure 1 show
 51 that the new axisymmetric design comprises sixteen,
 52 12 mm-wide concentric, PVC rings (the central one be-
 53 ing a 12 mm diameter cylinder). Each ring is 38 mm
 54 high and there is a 1 mm gap between adjacent rings
 55
 56
 57
 58
 59
 60
 61
 62
 63
 64
 65

for flexibility; the total radius of the generator is 201 mm.

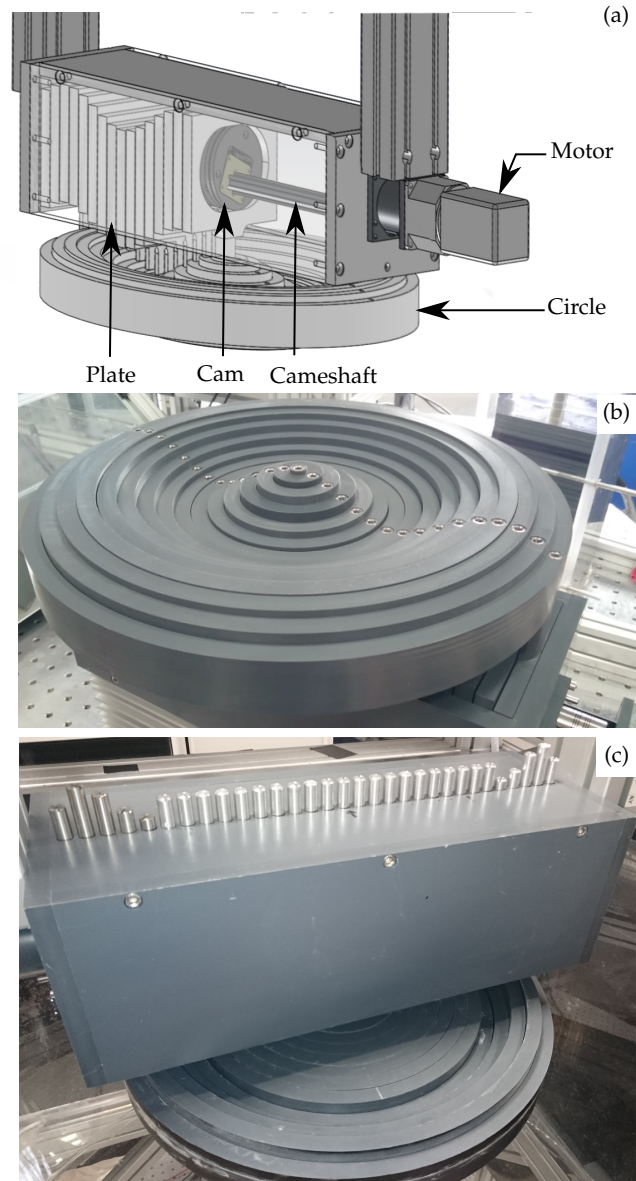


Fig. 1: (a) A schematic of the axisymmetric wave generator (with only half of the plates and cams shown, for clarity). The vertical motion of the rings is driven by the cams, which follow a sinusoidal motion at frequency ω imposed by the motor. (b) Underside view of the wave generator and (c) aluminum guides which horizontally constrain the plates, thus ensuring purely vertical motion of the rings.

In contrast to a two-dimensional generator, for which the movement of each plate is driven by a single cam,

each ring (with the exception of the central ring) is driven by two cams located equidistant from the central ring of the generator (see figure 1); this is necessary in order to enhance control and provide balance to the motion of the rings. To prevent jamming of the plates, aluminum guides (figure 1(c)) are used to ensure parallel, vertical motion.

Numbering the rings 1 to 16 from the center to the outer ring of the generator, their prescribed vertical motion is:

$$z_n(t) = z_{0,n} \cos(\omega t + \phi_n) \quad \forall n \in \llbracket 1, 16 \rrbracket, \quad (1)$$

where $z_{0,n}$ is the displacement amplitude of ring n (in the range 0-15 mm for our generator), ω is the rotational frequency of the camshaft, and ϕ_n is the phase of ring n (chosen by increments of $\pi/6$ for our generator). As an example, in order to force a concentric sinusoidal wave $z(r, t) = a \cos(\omega t - kr)$ with an arbitrary amplitude a , a horizontal wavelength $2\pi/\lambda$ chosen to be the width of six rings, and an outward propagating phase, the corresponding configuration of the cams would be:

$$z_{0,n} = a \quad \forall n \in \llbracket 1, 16 \rrbracket, \quad (2)$$

$$\phi_n = kr_n = 2n\pi/6 \quad \forall n \in \llbracket 1, 16 \rrbracket, \quad (3)$$

where r_n is the nominal radial position of ring n .

This novel geometry opens up a wide range of possibilities for the excitation of different types of internal wave fields in density stratified fluids. For example, an axisymmetric standing-wave pattern can be excited if all the phases of the plates are identical, or radially outward (inward) propagating waveforms result if the plate phases are increasing outward (inward). Imposing different amplitudes of oscillation for different rings allows for scenarios such as a strong disturbance in the center of the domain that decreases smoothly towards the outer domain.

We also note that by virtue of its geometry the device is well suited for generating purely inertial waves in rotating systems. Since the possibilities are plentiful, our goal in this paper is to provide the first demonstration of the capabilities of such a generator by visualizing some examples of inertia-gravity wave fields excited using this technology. We leave it to the interested reader to further explore the broad possibilities.

2.2 Experimental arrangement

Our experiments were conducted in a cylindrical plexiglas tank that was housed within a transparent plexiglas tank of square cross section (see figure 2). Salt

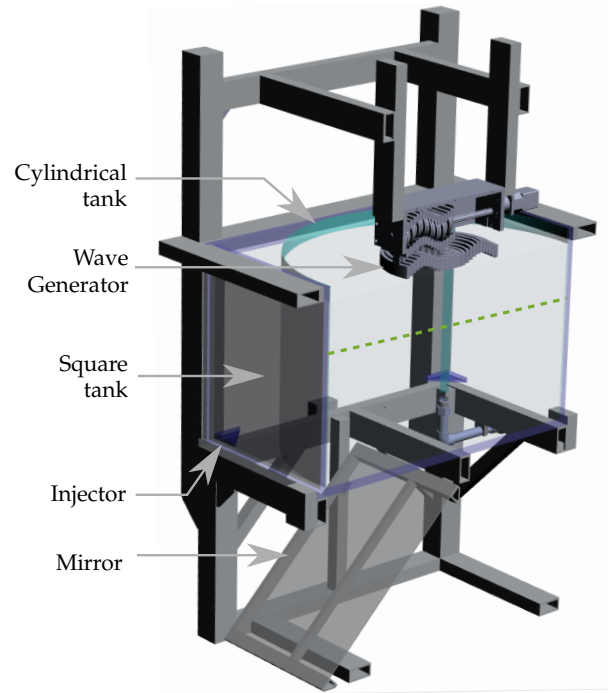


Fig. 2: Cross-sectional schematic of the experimental system comprising a transparent cylindrical tank within a square tank. The wave generator is placed above the tank, centered on the axis of rotation. The green dashed line shows the approximate position of the horizontal laser sheet in which horizontal wave velocities are measured by PIV, viewed via the tilted mirror beneath the experimental tank.

stratified water resided both inside and outside of the cylinder, preventing significant optical deformations for the visualization system. In setting the scale of the system, an important consideration was that viscous damping for inertia-gravity waves scales as the cube of the wavevector amplitude. To try and lessen the impact of viscous damping, our square external tank had sides of length 1 m, enabling the inner cylindrical tank to be 1 m in diameter; both tanks were 0.6 m in height. A series of horizontal holes were drilled around the lower section of the cylindrical tank to allow fluid to flow freely between the two chambers during filling from below.

The tank structure was mounted on a turntable (denoted as PERPET, designed and constructed by GP Concept) that was 1.92 m in diameter. The rotational velocity could be set in the range $0 < \Omega < 60$ rpm with an accuracy of 0.1%, which corresponds to a Coriolis parameter $f = 2\Omega$ in the range $0 < f < 12.5 \text{ rad} \cdot \text{s}^{-1}$. The axis of rotation was vertically aligned with gravity with a tolerance of $2 \text{ mm} \cdot \text{m}^{-1}$. A salt stratification was established using the standard double bucket method

(Fortuin, 1960; Oster and Yamamoto, 1963) with buoyancy frequency $N \approx 1 \text{ rad} \cdot \text{s}^{-1}$.

The tank was filled while at rest and then spun up very slowly, at an angular acceleration rate less than $10^{-3} \text{ rad} \cdot \text{s}^{-2}$, in order to prevent mixing from degrading the stratification. Since a vertical density gradient suppresses vertical fluid motion, the typical time scale to achieve solid body rotation is longer for a stratified fluid than for a homogeneous fluid, for which three-dimensional flows such as Ekman pumping distribute momentum from the rotating base of the tank into the body of the fluid that is initially at rest. In the most extreme case, a body of stratified fluid will be set in rotation by viscosity alone. In this case, assuming that the flow is purely azimuthal and that there is no variation of the velocity in z (case of an infinitely high cylinder), the azimuthal velocity v_θ is the solution to:

$$\frac{\partial v_\theta}{\partial t} = \nu \Delta v_\theta, \quad (4)$$

where ν is the kinematic viscosity. Figure 3 (a) presents histories of the horizontal velocity at a point in the bulk ($r = 29 \text{ cm}$) undergoing external rotation (in the case of the stratified fluid, the horizontal velocity $v_h = \sqrt{v_\theta^2 + v_r^2}$ reduces to v_θ , since radial motion is negligible). Once the momentum induced by the rotation of the tank walls is fully diffused, we expect the velocity to vanish in the rotating frame. As expected, the momentum diffusion time was notably shorter for a homogeneous fluid (~ 2.5 hours) than for a stratified fluid (~ 15 hours). The solution to equation (4) (assuming a no slip boundary condition and $r = 29 \text{ cm}$ - the radius where the velocity was measured) is included in figure 3(a) and is in good agreement with the measurements for a stratified fluid; viscosity is therefore the dominant force that drives the stratified fluid into rotation. Furthermore, the stratified experiments confirmed that radial velocity is negligible in comparison to the azimuthal velocity, which confirms the applicability of equation (4). To demonstrate the minimal impact of spin-up on the initial stratification, figure 3(b) presents an example of a density profile before rotation, after spin-up of the table, and after 16 hours of constant rotation at $\Omega = 0.125 \text{ rad} \cdot \text{s}^{-1}$. It is clear that even on a timescale much larger than the typical experimental time ($\sim 20 \text{ min}$), the variation of N is negligible.

Particle Image Velocimetry (PIV) was used to measure the experimental velocity field. A laser sheet was created by passing a 2 Watt Ti:Sapphire laser (Laser Quantum) with a 532 nm wavelength through a cylindrical lens. The laser sheet could be oriented both vertically and horizontally, with the former passing

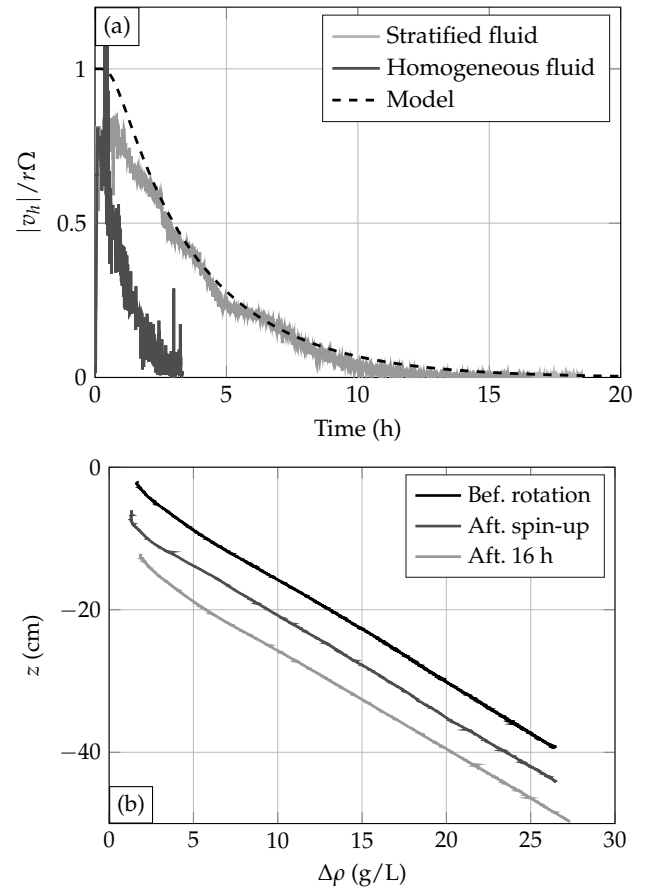


Fig. 3: (a) Magnitude of the horizontal velocity of the fluid $|v_h|$ (in the stratified case, $v_h \simeq v_\theta$) for the flow at radius $r = 29 \text{ cm}$ while the turntable is spun up to a rotation rate $\Omega = 0.125 \text{ rad} \cdot \text{s}^{-1}$, for a homogeneous (black line) and a stratified (gray line) fluid. In the case of the stratified fluid, the measurements are in agreement with the solution to equation (4) (dashed line), which only considers the viscous diffusion of momentum from the sidewalls. (b) A sample stratification measured before rotation, after the turntable has completed its acceleration to an angular velocity of $\Omega = 0.125 \text{ rad} \cdot \text{s}^{-1}$ in 240 s, and after 16 hours of rotation at constant angular velocity $\Omega = 0.125 \text{ rad} \cdot \text{s}^{-1}$; a vertical offset of 5 cm has been introduced between the three profiles to aid visual comparison.

through the central axis of the rotation table (with visualization taking place through a normal facing side of the tank), and the latter requiring visualization through the tank base via a 45° inclined mirror (see figure 2). When the laser sheet was positioned vertically, the fluid was seeded with a concentration of $3.3 \text{ mg} \cdot \text{L}^{-1}$ of hollow glass spheres (manufactured by Sphericell, with $1.1 \text{ kg} \cdot \text{L}^{-1}$ density, and $10 \mu\text{m}$ diameter); when the laser sheet was oriented horizontally,

1 the fluid was seeded with a concentration of $0.8 \text{ mg} \cdot \text{L}^{-1}$
 2 of silver coated hollow glass spheres (manufactured by
 3 Dantec Dynamics, with 1.4 kg L^{-1} density, and $10 \text{ }\mu\text{m}$
 4 diameter). Experiments involving a horizontal laser
 5 sheet require seed particles with more reflectivity given
 6 that the scattered light has to travel through the 3 cm
 7 thick tank bottom, which oftentimes has a layer of sed-
 8 imented particles above it. The CIVx algorithm (Fin-
 9 cham and Delerce, 2000) was used to compute the cross-
 10 correlation between two successive images, giving, in
 11 the case of the vertical sheet, the instantaneous vertical
 12 and radial velocities, and in the case of the hori-
 13 zontal sheet, the instantaneous azimuthal and radial
 14 velocities. The maximum opening angle of the camera
 15 relative to the laser sheet was 20° , which largely sup-
 16 pressed parallax. Moreover, a sufficiently high image
 17 acquisition rate was chosen ($\sim 4 \text{ Hz}$) in order to min-
 18 imize the out-of-plane particle displacement between
 19 successive images. Images were recorded using a Al-
 20 lied Vision Pike F-505 camera (maximal resolution of
 21 $2452 \text{ (H)} \times 2054 \text{ (V)}$) and 12.5 mm focal lens located
 22 at 130 cm from the middle of the tank, leading to a
 23 0.36 mm/pixel resolution and a maximum field of view
 24 of $88 \times 74 \text{ cm}^2$.

30 Analytical Model

31 To investigate the quality of the wave fields produced
 32 by the wave generator, we consider an axisymmetric
 33 model of inertia-gravity wave generation and propa-
 34 gation in the presence of a background stratification,
 35 $N(z)$, and background rotation, f . In contrast to two-
 36 dimensional models, for which the horizontal basis func-
 37 tions are naturally Fourier modes (Mathur and Pea-
 38 cock, 2009), an axisymmetric system is characterized
 39 by Bessel functions. Figure 4 presents a schematic of
 40 the basic geometry of a wave field that originates from
 41 an axisymmetrically configured generator driven at a
 42 fixed frequency, ω , in a linear stratification (*i.e.* con-
 43 stant N). In such a configuration the inertia-gravity
 44 waves are emitted at a fixed angle β (defined in fig-
 45 ure 4) relative to the horizontal according to the inertia-
 46 gravity wave dispersion relation:

$$51 \quad \omega^2 = N^2 \sin^2 \beta + f^2 \cos^2 \beta. \quad (5)$$

56 3.1 Governing equations

57 Small-amplitude, axisymmetric inertia-gravity waves
 58 in a viscous, Boussinesq, density-stratified fluid with

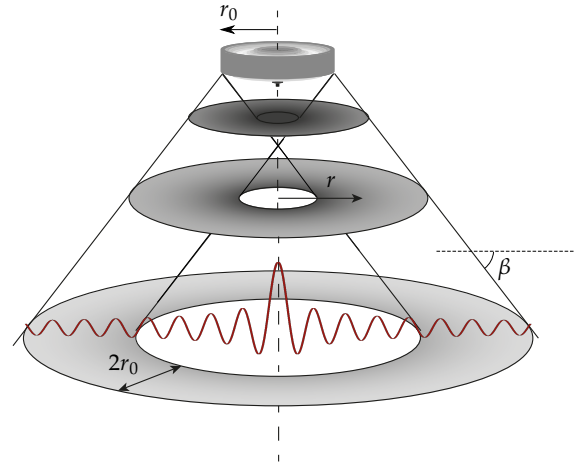


Fig. 4: A schematic illustrating the structure of the ver-
 tical velocity component of an inertia-gravity wave
 field radiated at a fixed frequency ω in a constant N
 stratification, subject to the dispersion relation (5). For
 an initial forcing of radius r_0 the wave field is ex-
 pected to primarily reside within a ring of width $2r_0$.
 An example Bessel function wave form is presented in
 red, showing the expected decrease of the amplitude,
 which scales as $r^{-1/2}$, as the wave propagates down-
 ward and outward with increasing r .

constant background rotation satisfy the following sys-
 tem of governing equations:

$$59 \quad \partial_t v_r = f v_\theta - \frac{1}{\rho_0} \partial_r p + \nu \Delta_h v_r, \quad (6)$$

$$60 \quad \partial_t v_\theta = -f v_r + \nu \Delta_h v_\theta, \quad (7)$$

$$61 \quad \partial_t v_z = -\frac{\rho'}{\rho_0} g - \frac{1}{\rho_0} \partial_z p + \nu \Delta_z v_z, \quad (8)$$

$$62 \quad \partial_t \rho' = \frac{v_z N(z)^2 \rho_0}{g}, \quad (9)$$

$$63 \quad 0 = \frac{1}{r} \partial_r (r v_r) + \partial_z v_z, \quad (10)$$

where $\mathbf{v}(r, z, t) = (v_r, v_\theta, v_z)$ is the velocity field with
 radial (r), azimuthal (θ) and vertical (z) components,
 ρ' is the perturbation to the background density $\bar{\rho}(z)$, p
 is the pressure perturbation, $N(z) = \sqrt{(-g/\rho_0) \partial \bar{\rho} / \partial z}$ is
 the background buoyancy frequency, ρ_0 is a reference
 background density and $f = 2\Omega$ is the Coriolis fre-
 quency for a given background rotation frequency Ω .
 Δ_h represents the vector laplacian projected in the hori-
 zontal (radial or orthoradial) directions, while Δ_z is
 the vector laplacian in the axial direction.¹ We assume

¹ The mathematical expressions for the vector laplacian of X
 in the cylindrical coordinates are $\Delta_h X = \frac{\partial^2 X}{\partial z^2} + \frac{\partial^2 X}{\partial r^2} + \frac{1}{r} \frac{\partial X}{\partial r} - \frac{X}{r^2}$
 and $\Delta_z X = \frac{\partial^2 X}{\partial z^2} + \frac{\partial^2 X}{\partial r^2} + \frac{1}{r} \frac{\partial X}{\partial r}$

the absence of any azimuthal variation i.e. $\partial_\theta \approx 0$; this assumption does not prohibit the existence of an azimuthal velocity component v_θ , as will be shown later.

Using the combined equations ∂_{tz} (6), (7), ∂_{tr} (8) and (9), and eliminating common terms between these four equations, we obtain ²:

$$\partial_{ttz}v_r - \partial_{ttr}v_z = N(z)^2\partial_rv_z - f^2\partial_zv_r + \nu\Delta_h(\partial_{tz}v_r - \partial_{tr}v_z + f\partial_zv_\theta). \quad (11)$$

Furthermore, introducing an axisymmetric stream function Ψ that satisfies (10),

$$v_r = -\frac{1}{r}\partial_z(r\Psi), \quad (12)$$

$$v_z = \frac{1}{r}\partial_r(r\Psi), \quad (13)$$

equation (11) becomes

$$-\partial_{tt} \left[\partial_{zz}\Psi + \partial_r \left(\frac{1}{r}\partial_r(r\Psi) \right) \right] = N(z)^2\partial_r \left(\frac{1}{r}\partial_r(r\Psi) \right) + f^2\partial_{zz}\Psi + \nu\Delta_h \left[-\partial_{tzz}\Psi - \partial_{tr} \left(\frac{1}{r}\partial_r(r\Psi) \right) + f\partial_zv_\theta \right]. \quad (14)$$

Any axisymmetric wave field can be decomposed into a sum of products of Bessel functions and sine functions since the linearity of the governing equations allows for each of these modes to be independently studied; we therefore take Ψ to be a harmonic solution incorporating a radial first order Bessel function, J_1 :

$$\Psi(z, r, t) = \psi(z)J_1(kr) \exp(-i\omega t), \quad (15)$$

where $\psi(z)$ is the vertical structure of the wave field. We make this choice rather than a zeroth order Bessel functions because we must have $v_r = 0$ at $r = 0$, otherwise mass conservation is not satisfied. Furthermore, this decomposition reduces the Laplacian operator, Δ_h , to

$$\Delta_h\Psi = -k^2\Psi + \partial_{zz}\Psi. \quad (16)$$

Combining equations (12) and (13) with well-known relations between Bessel functions and their derivatives, the velocities are expressed as:

$$v_r = -\psi'(z)J_1(kr) \exp(-i\omega t), \quad (17)$$

$$v_z = k\psi(z)J_0(kr) \exp(-i\omega t). \quad (18)$$

² Note that, mathematically $\partial_r\Delta_z = \Delta_h\partial_r$.

3.2 Inviscid solution

In the inviscid case, v_θ is given by

$$v_\theta = \frac{-if}{\omega}\psi'(z)J_1(kr) \exp(-i\omega t), \quad (19)$$

and equation (14) becomes

$$\psi''(z)(-\omega^2 + f^2) + \psi(z)k^2(\omega^2 - N(z)^2) = 0. \quad (20)$$

For a constant stratification (i.e. $N(z) = N_0$), the solution of this equation is proportional to $\exp(imz)$, with the vertical wavenumber m satisfying the dispersion relation:

$$m(k, \omega) = \pm k \left(\frac{N_0^2 - \omega^2}{\omega^2 - f^2} \right)^{1/2}. \quad (21)$$

We note that equation (21) corresponds to the dispersion relation in equation (5), where $\beta = \arctan(k/m)$. Thus, the general solution for equation (14), in the inviscid limit, is of the form:

$$\Psi = \Psi_0 \exp(imz)J_1(kr) \exp(-i\omega t), \quad (22)$$

where Ψ_0 is a constant wave amplitude.

3.3 Weakly viscous solution

In our experiments, viscous effects are small but not entirely negligible. The following derivation takes viscosity into account at first order in $\epsilon = \nu k^2/\omega \ll 1$. Since v_θ , described at order zero by equation (19), appears only at first order in equation (14), incorporating a viscous correction in v_θ would yield an unnecessary second order correction. It is thus sufficient to keep v_θ at zero order (without a viscous correction) via equation (19).

Inserting equation (15) into equation (14) and using equation (19) for v_θ yields the fourth differential equation

$$\psi''''(z)iv \left[\omega - \frac{f^2}{\omega} \right] + \psi(z)k^2[\omega^2 - N(z)^2 + iv\omega k^2] + \psi''(z) \left[-\omega^2 + f^2 - ivk^2 \left(2\omega - \frac{f^2}{\omega} \right) \right] = 0. \quad (23)$$

Equation (20) is the limiting case ($\nu = 0$) of equation (23).

For a constant stratification ($N(z) = N_0$) and in the presence of weak viscosity, the modal solutions have the approximate form

$$\Psi = \Psi_0 \exp(i\mathcal{M}z) J_1(kr) \exp(-i\omega t), \quad (24)$$

where

$$\mathcal{M}(k, \omega) = m(k, \omega) + \epsilon m^\nu(k, \omega), \quad (25)$$

m is the inviscid vertical wavenumber given by (21), and m^ν is a weakly viscous correction. The explicit expression for this term is

$$m^\nu(k, \omega) = \frac{\mp ik}{2(\omega^2 - f^2)(N_0^2 - \omega^2)} \sqrt{\frac{\omega^2 - N_0^2}{f^2 - \omega^2}}. \quad (26)$$

From this expression, we can compute that for all the experiments to be compared with the model, the typical viscous dissipation length is generally of the order of a few meters, therefore we can conclude that viscous effects do not play a major role in these experiments. For this reason, we use the inviscid model in what follows.

3.4 General solution

The modal solutions presented in the previous section enable a standard procedure to predict the entire wave field in an experimental domain, using its radial structure at a given depth as a boundary condition. From a time series of the vertical velocity at a given depth (which we take to be $z = 0$), one computes the Fourier-Hankel transform in space and time; this transform gives a measurement of the amplitude of each temporal and spatial mode $\tilde{\Psi}_{k,\omega}(z = 0)$. Note that we use the time series of the vertical velocity component, rather than the radial velocity component, in order to obtain a direct measurement of Ψ (see equation (18)).

In the case of a constant stratification, which is the scenario we consider in this paper, the solution is given by the propagation of each mode $\tilde{\Psi}_{k,\omega}$ according to equation (24), yielding

$$\Psi(z, r, t) = \sum_{k,\omega} \tilde{\Psi}_{k,\omega}(z = 0) \exp[i\mathcal{M}(k, \omega)z] J_1(kr) \exp(-i\omega t). \quad (27)$$

More generally, in an arbitrary stratification, each mode $\tilde{\Psi}_{k,\omega}(z)$ propagates according to equation (23) and the formal solution is:

$$\Psi(z, r, t) = \sum_{k,\omega} \tilde{\Psi}_{k,\omega}(z) J_1(kr) \exp(-i\omega t). \quad (28)$$

4 Results

We investigated two different types of forcing: one with a radial profile of a Bessel function, and a second type of forcing mimicking an axisymmetric bump, which we refer to as a *Bourrelet* configuration. As we have shown in the previous section, the first configuration, that of the Bessel function, is a natural mode to describe axisymmetric wave fields. The second configuration i.e. the Bourrelet, enables geometric focusing which has the propensity to yield intriguing nonlinear effects.

4.1 Bessel function forcing.

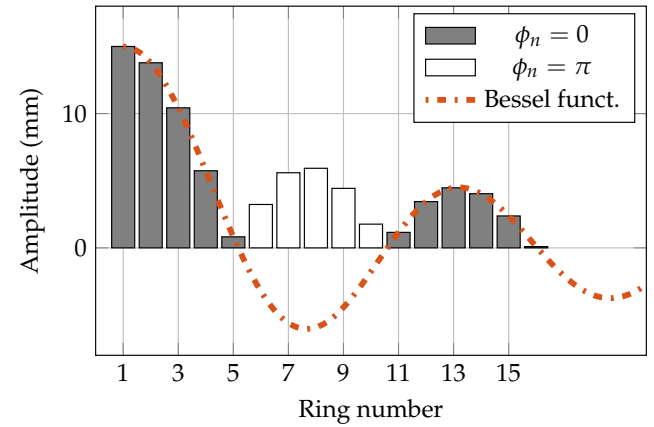


Fig. 5: Amplitudes and phases of the cams for the Bessel function configuration. The dashed orange line represents the Bessel function used to calculate the plate amplitude with a wavenumber $k_{\text{gen}} = 42 \text{ m}^{-1}$.

This configuration aims at reproducing a zeroth order Bessel function for the vertical velocity, although the finite extent of the generator naturally results in a mildly truncated Bessel function. To keep the spatial scale large enough that viscous effects are weak, we chose to reproduce the Bessel function over one and a half "wavelengths"; figure 5 shows the amplitude and phase designated to each ring. The profile was scaled with an amplitude of 15 mm for the center ring.

Cross sections of the vertical and radial velocity components of the wave field, obtained in the vertical plane containing the central axis of the generator ($r = 0$), are presented in figure 6. The symmetry and antisymmetry of the respective vertical and radial velocity fields, with respect to the $r = 0$ centerline, as reflected in equations (17) and (18), can be clearly observed. Along the $r = 0$ centerline, the vertical ve-

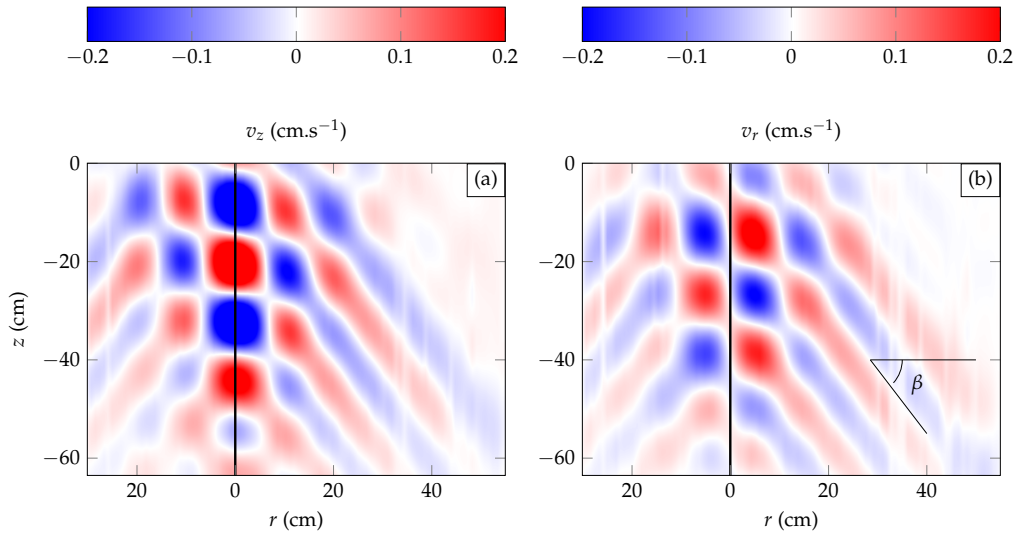


Fig. 6: PIV images of the (a) vertical and (b) radial velocity fields for a wave field radiating from a generator (located at $z = 0$ and centered at $r = 0$) configured with the Bessel function form presented in figure 5: $k_{\text{gen}} = 42 \text{ m}^{-1}$, $a=15 \text{ mm}$ for the center ring, $\omega/N = 0.79$ and $f/N = 0.2$.

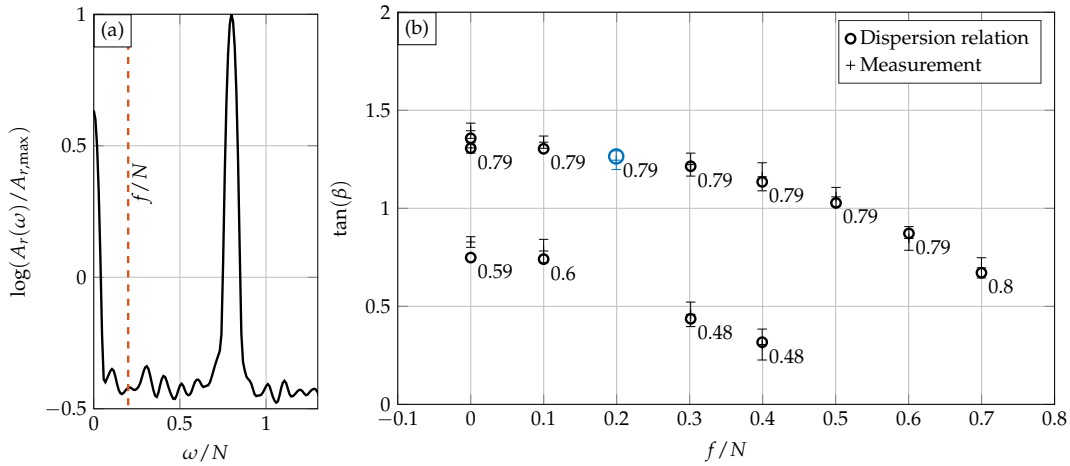


Fig. 7: (a) Temporal Fourier transform of the radial velocity, measured in a vertical plane (for the same wave shown in figure 6) over 500 images, corresponding to a 250 s time window. The dashed line represents $\omega/N = f/N = 0.2$. (b) A comparison of the direct measurement of $\tan \beta$ from spatial images like those shown in figure 6, and the expected values of $\tan \beta$ using the dispersion relation (21); the value of ω/N used for each experiment is indicated next to each data point. The larger blue circle in (b) shows the experiment of figure 6 and figure 10.

locity is a decaying sinusoid, as expected for an outward propagating Bessel function. Outside of the central region of the domain, the wave field is oriented at an angle β with respect to the horizontal. This clearly defined angle is a sign of temporal monochromaticity, which is further confirmed by the frequency spectrum of the wave field (presented in figure 7(a)).

From snapshots of the wave field, we can confirm the expected dispersion relation (5) for the generated

waves. With N and f known, the angle β can be extracted directly from the velocity snapshots by plotting the iso-phase lines, while ω can be confirmed by obtaining a temporal Fourier spectrum from the time histories, such as that presented in figure 7(a). As shown in figure 7(b), the measured $\tan \beta$ quantity, determined using spatial images like those shown in figure 6, and the expected $\tan \beta$ quantity, determined via the dispersion relation given by equation (21), are in excellent agreement across a wide number of experiments with

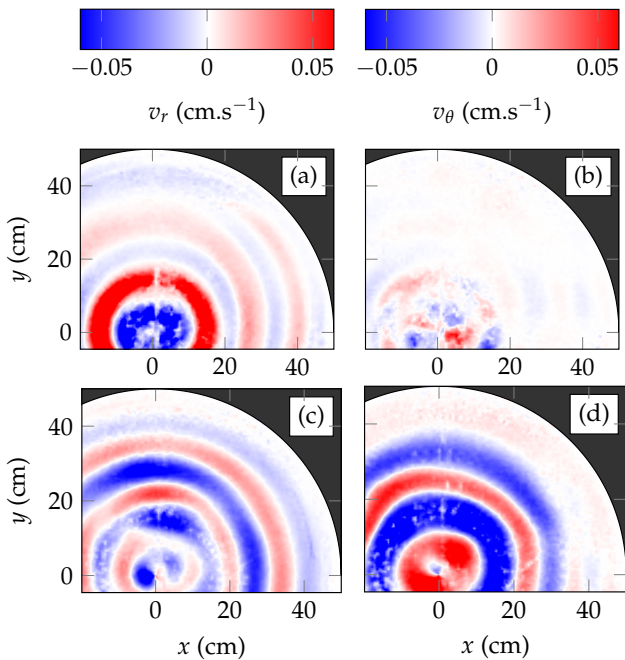


Fig. 8: Wave field velocities in the horizontal plane at $z = 10$ cm; the wave generator, forcing at $\omega/N = 0.5$, is centered at $(x, y) = (0, 0)$ cm. The left and right columns depict the radial and azimuthal velocity fields, respectively; panels (a,b) have no rotation, whereas (c,d) correspond to $f/N = 0.3$. The area shaded black is external to the experimental cylinder.

varying values of ω/N and f/N . As such, we conclude that the wave field produced by the generator is indeed propagating according to the linear inertia-gravity waves dispersion relation, as expected.

Next we consider the horizontal structure of the wave field, with the goal of checking the axisymmetry, as well as the existence of an azimuthal velocity component; the experimental setup allows for such observations through the use of a 45° mirror. Figure 8 presents velocity field measurements obtained in a horizontal plane 10 cm below the generator. As expected, the velocity field is indeed quite axisymmetric, although with some minor imperfections. In the non-rotating case, the azimuthal velocity is negligible, whereas in the rotating case it is well established, as predicted by equation (19). Comparing figures 8(a) and 8(c), one can also observe that the radial decay appears stronger in the non-rotating case; this is due to the more shallow propagation angle of waves in the rotating case, which results in a larger overlap between the intersecting image plane and the wave cone..

In further assessing the Bessel-function nature of the radiated wave field, we note that the forcing was

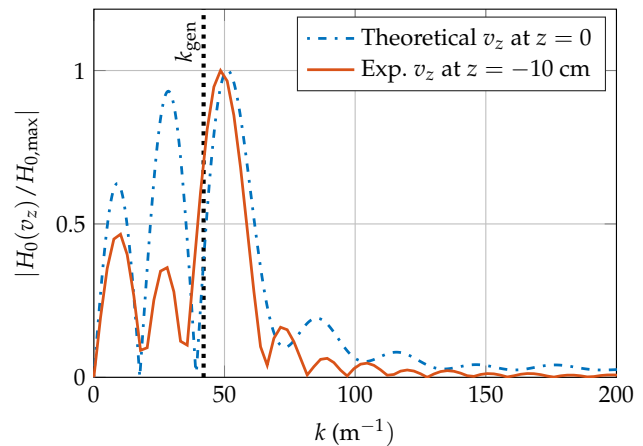


Fig. 9: Hankel transform of the truncated Bessel function used for the wave generator profile (dashed-dotted blue line), and the radial profile of the vertical velocity at $z = -10$ cm (solid red line). The black dotted line shows the value k_{gen} of the Bessel function used to set the wave generator profile.

actually not a true Bessel function, but rather a truncated Bessel function due to the absence of experimental forcing for $r > 20$ cm. To investigate the effect of this truncation, we compared the Hankel transforms of the wave generator profile and the radial profile of a typical experiment, the result of which is presented in figure 9. The Hankel transform of a pure Bessel function is simply an isolated peak at k_{gen} , whereas truncation of the Bessel function beyond the first couple of wavelengths introduces several secondary peaks while maintaining a dominant peak around k_{gen} in the corresponding Hankel transform. The Hankel transform of the experimental radial profile of v_z at $z = -10$ cm displays the same characteristics associated to the truncated Bessel function, with particularly nice agreement at the primary peak closest to k_{gen} . The two peaks at $k < k_{\text{gen}}$ are also present, although with smaller amplitudes compared to the theoretical peaks. Interestingly, the transform of the experimental profile does not show any peak around $k = 500 \text{ m}^{-1}$ (not shown in the figure), which corresponds to the thickness of the individual rings that make up the wave generator. This confirms that the discretization of the forcing profile via plates of finite thickness has negligible impact on the generated wave field, in line with the findings of Mercier et al. (2010).

We now use the procedure described in section 3, in particular equation (27), to make direct comparisons between our axisymmetric model and experiments. To begin, we recorded a time series of the vertical velocity at a depth 10 cm below the generator. This particular

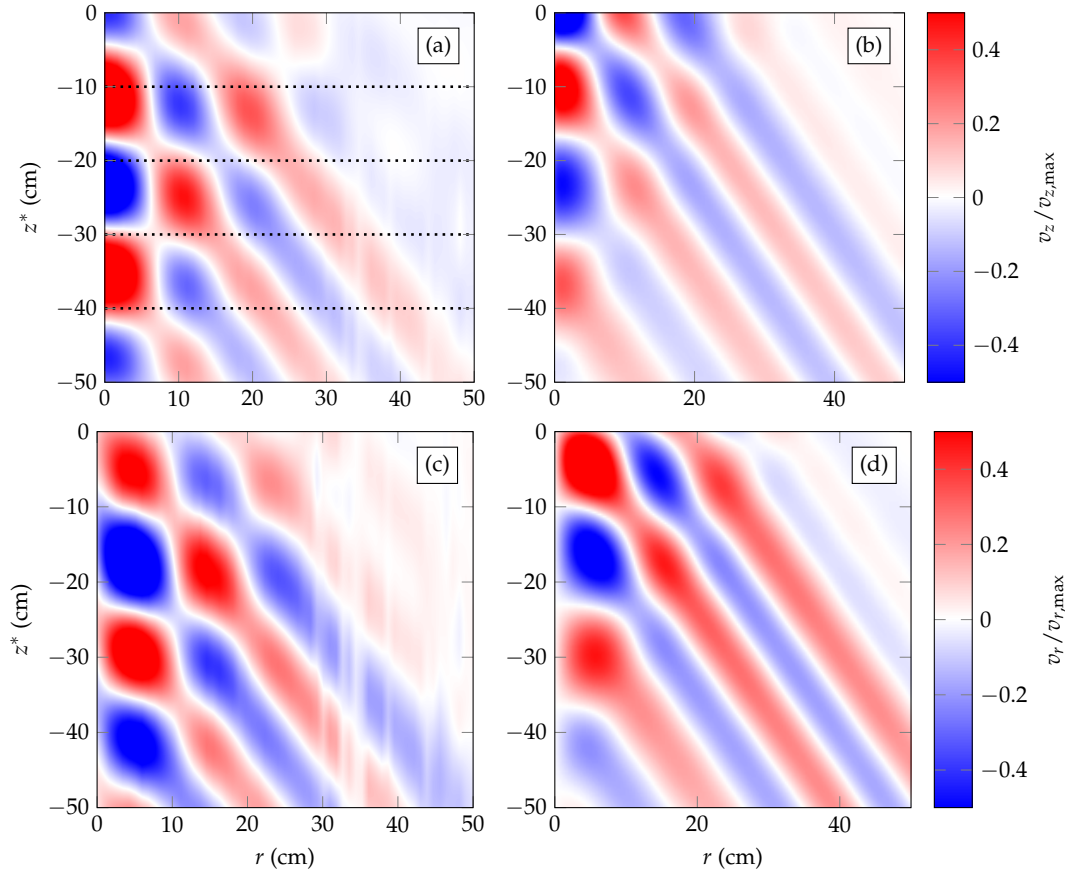


Fig. 10: Experimental measurements of the vertical (a) and radial (c) velocities in a vertical plane passing through the central axis of the generator. (b), (d) Corresponding theoretical predictions using equation (27). The generator is set as a Bessel function, with $\omega/N = 0.79$ and $f/N = 0.2$. Dashed lines represent the vertical levels used to plot the amplitude envelopes presented in figure (11). Note that the vertical axis is $z^* = z + 10$ in cm; the generator is therefore located at $z^* = 10$ cm.

depth was chosen because it was not too far from the generator while close enough to provide reliable measurements. Closer to the generator the wave cone is not as clean because of the mixing and mean current induced by the motion of the generator. For modeling purposes, this depth was set to be $z = 0$ and the resulting wave field below this vertical level was calculated using equation (27). Figure 10 presents a comparison of the experimental and theoretical velocity fields in a vertical plane. Overall, the analytical solutions compare very favorably to the experimental observations, except for small scale features which we attribute to measurement noise in the experimental data. More detailed comparisons involving velocity field profiles are presented in figure 11, which plots radial profiles of the radial and vertical velocities obtained at depths $z^* = -10, -20, -30$ and -40 cm. There is, as expected, a very close match at $z^* = -10$ cm, which is the profile positioned closest to the wave generator. We observe

consistently good agreement between theory and experiment over the four depths studied, with one notable difference being the prediction of the vertical velocity near the centerline at $z^* = -20$ cm. There are several possible reasons for this observed difference, including a slight non-axisymmetric nature of the experimental wave field due to an offset of the generator or a weak background flow, whether naturally present in the rotating tank or induced by the forcing of the generator.

Lastly, we investigate the efficiency of the wave generator in transmitting waves to the fluid bulk. This efficiency can be defined as the ratio between the induced wave vertical velocity $v_z(z_0)$, measured at a given depth z_0 , and the imposed generator vertical velocity amplitude $a\omega$, where a is the generator Bessel amplitude a . In order to neglect viscous damping, measurements were obtained at depth $z_0 = -5$ cm, the closest position where we could obtain reliable PIV data.

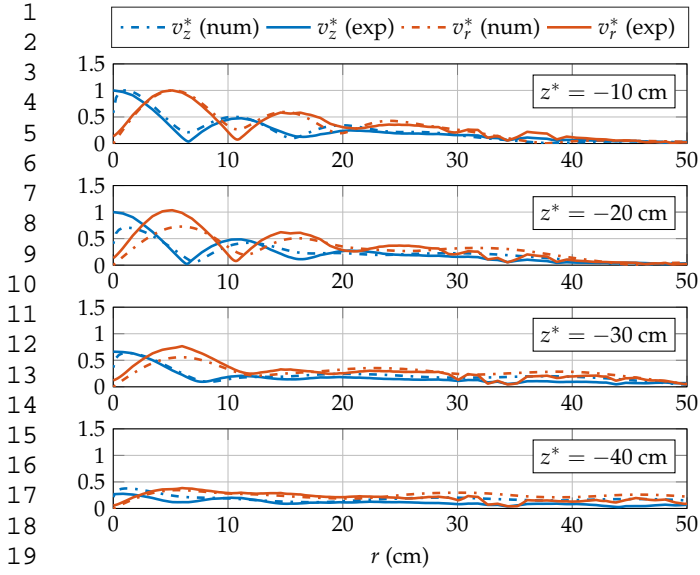


Fig. 11: Comparisons of experimental and theoretical amplitude envelopes of vertical and radial velocities, v_z^* and v_r^* , at $z^* = -10, -20, -30,$ and -40 cm (for the experiment shown in figure 10). Data has been normalized by the peak amplitude at $z = -10$ cm. Solid and dashed lines represent theoretical and experimental velocities, respectively.

Based on the computation of the viscous correction m^v expressed in equation (26), most data points in this measurement are unaffected by viscous effects, except the points at lowest frequency ω/N (below 0.4), which can explain the relative decrease of efficiency (compared to the theoretical curves) for these data points. Our results are presented in figure 12 as a function of forcing frequency for three different background rotation rates. At constant f , the efficiency increases with ω , related to the fact that the waves are more vertical and therefore more aligned with the motion of the generator rings. At constant ω , the efficiency decreases with background rotation. An increase in the background rotation rate yields a stronger azimuthal velocity field (as observed in figure 8d), and the accommodation of v_θ subsequently weakens the other two velocity components, v_r and v_z , thereby diminishing the efficiency of the wave generator. We note that the azimuthal velocity field is not imposed by the generator, but rather is induced by the external rotation. For an imposed vertical velocity $a\omega$, the maximum vertical velocity component as a function of f and ω is

$$V_{z,max} = a\omega \sqrt{\frac{\omega^2 - f^2}{N^2 - f^2}}. \quad (29)$$

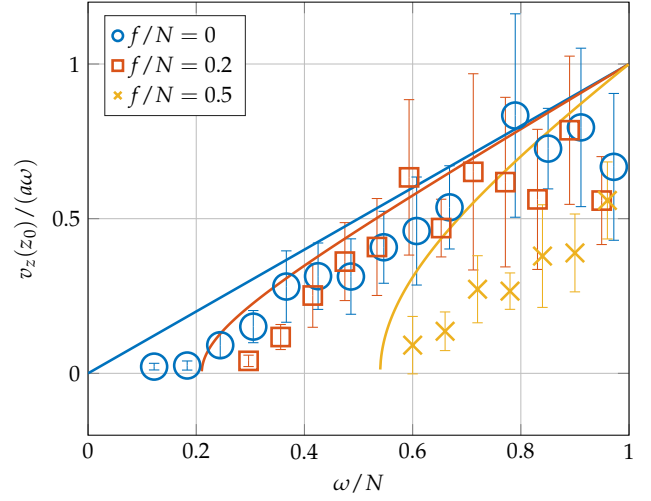


Fig. 12: Measurements of wave generator efficiency $v_z(z_0)/a\omega$ as a function of forcing frequency for three different background rotation rates. The solid lines represent $V_{z,max}/(a\omega)$.

From figure 12, we see that the measured efficiencies are consistently less than the maximum attainable efficiencies given by equation (29). Moreover, the difference between the two increases with growing background rotation, which is to be expected given how the experimental velocity field must adjust to accommodate an induced azimuthal component.

5 Le Bourrelet forcing

For our second experimental study, we considered the configuration of the generator shown in figure 13(a), in which the excitation is localized over four of the outer rings. This arrangement was chosen in order to produce a localized wave cone focused onto the central axis. Figure 13(b) shows that a generated wave cone will be subject to a large increase in intensity thanks to geometric focusing. It thus provides a novel way to create a controlled, intense, localized wave field that is the axisymmetric analog of the wave fields that have been studied by looking at colliding internal wave beams (Teoh et al., 1997; Smith and Crockett, 2014). While similar experiments have been performed using a vertically oscillating torus (Duran-Matute et al., 2013), our set-up allows for more controlled wave generation with respect to shape and amplitude.

Figures 14(a) and 14(c) present the vertical and radial velocities of the wave cones emitted from the *Bourrelet* arrangement; corresponding analytical solutions are presented in figures 14(b) and 14(d), respectively, following the same procedure described in section 4.

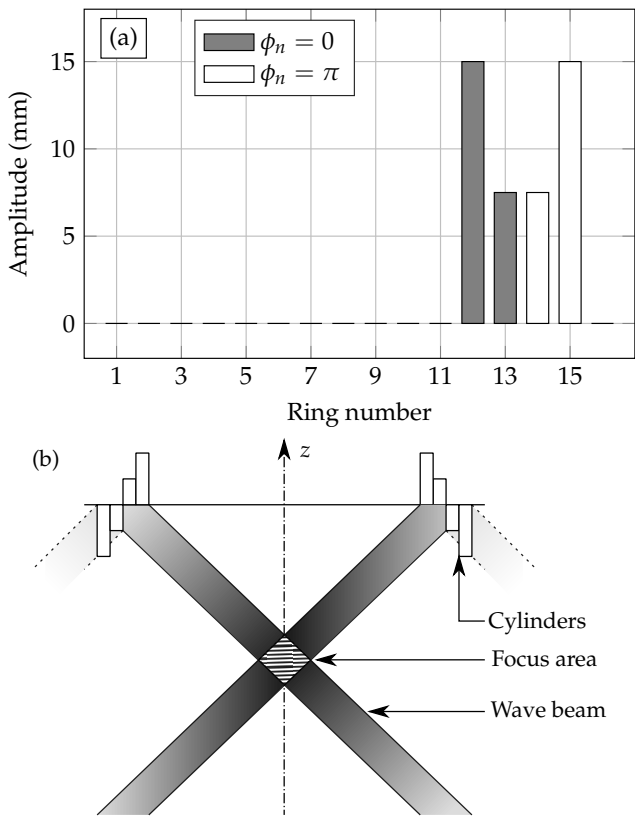


Fig. 13: (a) Amplitudes and phases of the cams for the wave generator set as a *Bourrelet*. (b) Schematic of the wave emitted from a *Bourrelet* and focus area where the amplitude of the wavefield is increased by geometric focusing.

The spatial frequencies of the *Bourrelet* is shown in figure 14(e). We observe good agreement between the spatial frequencies of the *Bourrelet* forcing and the vertical velocity field transmitted at $z = -10$ cm. As in the Bessel mode case, the wave generator successfully forms and transmits the desired wave structure. Because of the *Bourrelet* focusing that takes place, we expect nonlinear effects to take place. Indeed, in the highlighted dashed region, the theoretical solution, which does not take non-linear effect into account, differs significantly from the experimental wave field, (see figure 14(c)), where small-scale structures can be observed in the focal region. The actual study of this instability is, however, beyond the scope of this article.

6 Conclusion

Starting with the internal wave generator of Gostiaux et al. (2006), we advance the design by converting the plates into rings in order to generate axisymmetric inertia-gravity waves. Unlike other axisymmetric wave gen-

eration studies (Duran-Matute et al., 2013; Le Dizès, 2015), this system allows us to generate a controlled wave form by adjusting the amplitude and the offset of each cylinders. Starting with the decomposition of an axisymmetric internal wave field into its constituent Bessel modes, we model the linear propagation of the waves. We demonstrate the ability of the generator to produce two qualitatively different types of axisymmetric waves. The first is a truncated Bessel function for which PIV measurements in a horizontal and vertical plane were successfully collected. We demonstrate the quality of the wave generation in both a rotating and a non-rotating case. Moreover, we confirm the dispersion relation for various forcing and rotation frequencies, and we compare the emitted field with theory. The model and experimental wave fields are found to be in excellent agreement with the measured velocities. We also investigate the efficiency of the wave generator and find it to be operating reasonably close to maximum efficiency, with the exact degree of efficiency dependent on the external rotation rate.

The second configuration, which we name *le Bourrelet*, highlights the possibility of generating unique axisymmetric wave structures. One key feature of the *Bourrelet* is wave focusing. We show experimentally that, as wave focusing is established, the amplitude increase leads to wave instability.

Among the rich wave configurations and interactions offered by this new wave generator, some have caught our attention. To our knowledge, there is no mathematical description of internal wave instabilities in an axisymmetric context. Notably, the triadic resonant instability description would be challenging, as spatial resonance conditions are more complex when taking into account Bessel functions instead of plane waves. Our device is an interesting tool to emit a controlled Bessel mode and to study such kind of instability in an axisymmetric context, as was done previously with plane waves (Bourget et al., 2013; Ghaemsaïdi et al., 2016; Maurer et al., 2016). Future work could reproduce an axisymmetric “storm-like” forcing at the surface, to mimic the action of a storm on the ocean, which could subsequently yield experimental insight into wave propagation and mixing in a highly relevant geophysical context. The role of rotation in the propagation and mixing processes can also be investigated in our set-up, leading to geophysically relevant, complex experiments. Secondly, the *Bourrelet* configuration shows an interesting geometric focusing of a wave field that can be made more intriguing by altering the profile of the background stratification. For example, a non-uniform stratification can be used, where

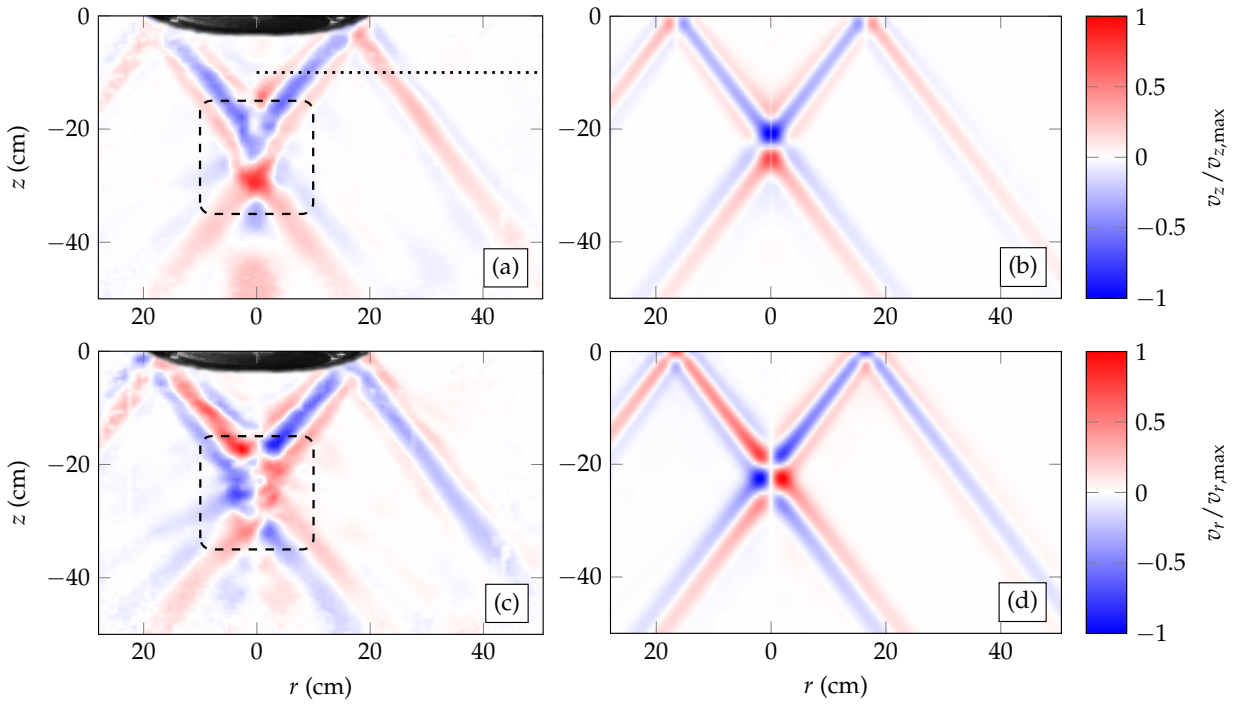


Fig. 14: Experimental measurements of the (a) vertical and (c) radial velocities in a vertical plane passing through the central axis of the generator. The generator is centered at $(z, r) = (0, 0)$ and set as a *Bourrelet*, with $\omega/N = 0.85$ and $f/N = 0.2$. The dashed square highlights the area where nonlinear effects are apparent. Corresponding linear predictions obtained using equation (27) are shown in panels (b) and (d).

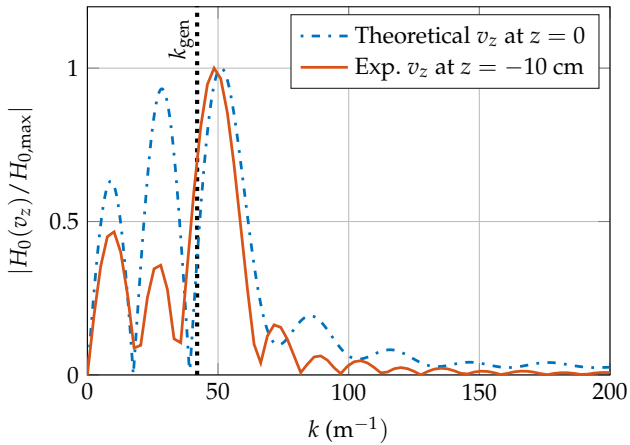


Fig. 15: Hankel transform (zero-th order) of both the vertical velocity profile at $z = -10$ cm (the location of the radial profile is shown in 14 (b) by a dotted line) and the corresponding theoretical profile (derived from the ring arrangement shown in figure 13(a)).

N changes with z , to tune the vertical transport of energy; the group velocity, which coincides with energy transmission, vanishes at z_0 , where $N(z_0) = \omega$ (Pao-

letti and Swinney, 2012). If the geometric focusing takes place at the same depth z_0 , we expect a significant accumulation of energy and the formation of a localized, highly nonlinear phenomenon.

We thank Neil Balmforth for insightful discussions. We thank M. Moulin and D. Le Tourneau for the design and production of the the wave generator and the tank. This work has been achieved thanks to the resources of PSMN from ENS de Lyon. The team in Lyon also thanks CNRS and ENS de Lyon for providing the financial support to build the rotating platform PERPET. T.P. acknowledges the support of the NSF (OCE-1357434).

References

- Apel J, Byrne H, Proni J, Charnell R (1975) Observations of oceanic internal and surface-waves from earth resources technology satellite. *J Geophys Res* 80(6):865–881. doi:{10.1029/JC080i006p00865}
- Bordes G, Venaille A, Joubaud S, Odier P, Dauxois T (2012) Experimental observation of a strong mean flow induced by internal gravity waves. *Physics of Fluids* 24(8):086602. doi:10.1063/1.4745880

- Bourget B, Dauxois T, Joubaud S, Odier P (2013) Experimental study of parametric subharmonic instability for internal plane waves. *Journal of Fluid Mechanics* 723:1–20. doi:10.1017/jfm.2013.78
- Cacchione D, Wunsch C (1974) Experimental study of internal waves over a slope. *Journal of Fluid Mechanics* 66(02):223. doi:10.1017/S0022112074000164
- Delisi DP, Orlanski I (1975) On the role of density jumps in the reflexion and breaking of internal gravity waves. *Journal of Fluid Mechanics* 69(3):445–464. doi:10.1017/S0022112075001516
- Duran-Matute M, Flór JB, Godeferd FS, Jause-Labert C (2013) Turbulence and columnar vortex formation through inertial-wave focusing. *Physical Review E - Statistical, Nonlinear, and Soft Matter Physics* 87(4):1–4. doi:10.1103/PhysRevE.87.041001
- Echeverri P, Flynn MR, Winters KB, Peacock T (2009) Low-mode internal tide generation by topography: an experimental and numerical investigation. *Journal of Fluid Mechanics* 636(6):91. doi:10.1017/S0022112009007654
- Fincham A, Delerce G (2000) Advanced optimization of correlation imaging velocimetry algorithms. *Experiments in Fluids* 29(7):S013–S022. doi:10.1007/s003480070003
- Fortuin JMH (1960) Theory and application of two supplementary methods of constructing density gradient columns. *J Polym Sci* 44(144):505–515. doi:10.1002/pol.1960.1204414421
- Ghaemsaidi SJ, Joubaud S, Dauxois T, Odier P, Peacock T (2016) Nonlinear internal wave penetration via parametric subharmonic instability. *Physics of Fluids* 28(1):011703. doi:10.1063/1.4939001
- Ghaemsaidi SJ, Peacock T (2013) 3D Stereoscopic PIV visualization of the axisymmetric conical internal wave field generated by an oscillating sphere. *Experiments in Fluids* 54(2):1454. doi:10.1007/s00348-012-1454-6
- Gortler H (1943) Über eine Schwingungserscheinung in Flüssigkeiten mit stabiler Dichteschichtung. *ZAMM Journal of Applied Mathematics and Mechanics / Zeitschrift für Angewandte Mathematik und Mechanik* 23(2):65–71. doi:10.1002/zamm.19430230202
- Gostiaux L, Didelle H, Mercier S, Dauxois T (2006) A novel internal waves generator. *Experiments in Fluids* 42(1):123–130. doi:10.1007/s00348-006-0225-7
- Halpern D (1971) Observations on short-period internal waves in Massachusetts bay. *Journal of Marine Research* 29(2):116
- Haury L, Briscoe M, Orr M (1979) Tidally generated internal wave packets in Massachusetts Bay. *Nature* 278(5702):312–317. doi:10.1038/278312a0
- Ivey G, Winters K, Koseff J (2008) Density Stratification, Turbulence, but How Much Mixing? *Annual Review of Fluid Mechanics* 40(1):169–184. doi:10.1146/annurev.fluid.39.050905.110314
- King B, Zhang HP, Swinney HL (2010) Tidal flow over three-dimensional topography generates out-of-forcing-plane harmonics. *Geophysical Research Letters* 37(14):n/a–n/a. doi:10.1029/2010GL043221
- Kunze E, MacKay C, McPhee-Shaw EE, Morrice K, Girton JB, Terker SR (2012) Turbulent Mixing and Exchange with Interior Waters on Sloping Boundaries. *J Phys Ocean* 42(6):910–927. doi:10.1175/JPO-D-11-075.1
- Le Dizès S (2015) Wave field and zonal flow of a librating disk. *Journal of Fluid Mechanics* 782(2015):178–208. doi:10.1017/jfm.2015.530
- Lee C, Beardsley R (1974) Generation of long nonlinear internal waves in a weakly stratified shear flow. *J Geophys Res Oceans* 79(3):453–462. doi:10.1029/JC079i003p00453
- Maas LRM, Benielli D, Sommeria J, Lam FPa (1997) Observation of an internal wave attractor in a confined, stably stratified fluid. *Nature* 388(6642):557–561. doi:10.1038/41509
- Mathur M, Peacock T (2009) Internal wave beam propagation in non-uniform stratifications. *Journal of Fluid Mechanics* 639:133. doi:10.1017/S0022112009991236
- Maurer P, Joubaud S, Odier P (2016) Generation and stability of inertia-gravity waves. *Journal of Fluid Mechanics* 808(1):539–561. doi:10.1017/jfm.2016.635
- Maxworthy T (1979) Note on the internal solitary waves produced by tidal flow over a 3-dimensional ridge. *J Geophys Res Oceans and Atmospheres* 84(NC1):338–346. doi:10.1029/JC084iC01p00338
- Mercier MJ, Martinand D, Mathur M, Gostiaux L, Peacock T, Dauxois T (2010) New wave generation. *Journal of Fluid Mechanics* 657:308–334
- Moore CD, Koseff JR, Hult EL (2016) Characteristics of bolus formation and propagation from breaking internal waves on shelf slopes. *Journal of Fluid Mechanics* 791(02):260–283. doi:10.1017/jfm.2016.58
- Mowbray DE, Rarity BSH (1967) The internal wave pattern produced by a sphere moving vertically in a density stratified liquid. *Journal of Fluid Mechanics* 30(03):489. doi:10.1017/S0022112067001569
- Oster G, Yamamoto M (1963) Density gradient techniques. *Chem Rev* 63(3):257–268. doi:10.1021/cr60223a003
- Paoletti MS, Swinney HL (2012) Propagating and evanescent internal waves in a deep ocean model. *Journal of Fluid Mechanics* 706(7):571–583. doi:10.1017/jfm.2012.284

- 1 Peacock T, Mercier MJ, Didelle H, Viboud S, Dauxois T
2 (2009) A laboratory study of low-mode internal tide
3 scattering by finite-amplitude topography. *Physics*
4 *of Fluids* 21(12):1–4. doi:10.1063/1.3267096
- 5
6 Smith S, Crockett J (2014) Experiments on nonlinear
7 harmonic wave generation from colliding internal
8 wave beams. *Experimental Thermal and Fluid Sci-*
9 *ence* 54:93–101. doi:10.1016/j.expthermflusci.2014.
10 01.012
- 11 Teoh S, Ivey G, Imberger J (1997) Laboratory study
12 of the interaction between two internal wave rays.
13 *Journal of Fluid Mechanics* 336(01):91–122. doi:
14 10.1017/S0022112096004508
- 15
16 Thomas JA, Lerczak JA, Moum JN (2016) Horizontal
17 variability of high-frequency nonlinear internal
18 waves in Massachusetts Bay detected by an array
19 of seafloor pressure sensors. *J Geophys Res Oceans*
20 121(8):5587–5607. doi:{10.1002/2016JC011866}
- 21
22
23
24
25
26
27
28
29
30
31
32
33
34
35
36
37
38
39
40
41
42
43
44
45
46
47
48
49
50
51
52
53
54
55
56
57
58
59
60
61
62
63
64
65